Boundary-Layer Meteorology (2025) 191:38
https://doi.org/10.1007/s10546-025-00926-9

RESEARCH ARTICLE

Accounting for Ocean Waves and Current Shear in Wind Stress Parameterization

David G. Ortiz-Suslow[1] · **Nathan Laxague**[2,6] · **Jan-Victor Björkqvist**[3] · **Milan Curcic**[4,5]

Received: 24 December 2024 / Accepted: 2 July 2025

Abstract

The wind shear stress at the ocean surface drives momentum exchange across the air-sea interface regulating atmospheric and oceanic phenomena. Theoretically, the mean wind stress acts in a reference frame moving with the ocean surface; however, the relative motion between the air and ocean surface layers is conventionally neglected in bulk transfer formulae. Recent developments improving air-sea momentum flux quantification advocate for explicitly defining the air-sea relative wind, especially in the regime of low wind forcing, where surface currents may approach a significant fraction of the total wind speed. Yet, in practice, this new approach is typically applied using opportunistic definitions of the near-surface current. Here, we build on this recent work and propose a general framework for the bulk air-sea momentum flux that directly accounts for vertical current shear and surface waves in quantifying the stress at the interface. Our approach partitions the stress at the interface into viscous skin and (wave) form drag components, each applied to their relevant surface advections, which are quantified using the inertial motions within the sub-surface log layer and the modulation of waves by currents predicted by linear theory, respectively. The efficacy of this approach is demonstrated using an extensive oceanic dataset from the Coastal Endurance Array (Ocean Observatories Initiative) offshore of Newport, Oregon (2017–2023) that includes co-located measurements of direct covariance wind stress, directional wave spectra, and current profiles. As expected, our framework does not alter the overall dependence of momentum flux on mean wind forcing, and we found the largest impacts at relatively low wind speeds. Below 3 m s^{-1}, accounting for sub-surface shear reduced form drag variation by 40–50% as compared to a current-agnostic approach; as compared to a shear-free current, i.e., slab ocean, a 35% reduction in form drag variation was found. At this wind forcing, neglecting the currents led to systematically overestimating the form stress by 20 to 50%—an effect that could not be captured by using the slab ocean approach. This framework builds on the existing understanding of wind-wave-current interaction, yielding a novel formulation that explicitly accounts for the role of current shear and surface waves in air-sea momentum flux. This work holds significant implications for air-sea coupled modeling in general conditions.

Extended author information available on the last page of the article

Keywords Air-sea interaction · Momentum flux · Upper ocean shear · Wave-current interaction · Observational data

1 Introduction

Within the inertial sublayer of the atmospheric boundary layer (ABL) under neutral thermal stratification, the streamwise velocity may approach the classic logarithmic profile (Blackadar and Tennekes 1968):

$$U(z) - \mathcal{U}_0 = \frac{u_*}{\kappa} \ln\left(\frac{z + z_0}{z_0}\right), \tag{1}$$

where we are at sufficient height above the wall (z) such that the direct impacts of viscous dissipation are negligible. Here, u_* is the surface friction velocity, κ is von Kármán's constant, z_0 and $\mathcal{U}_0$ are the surface roughness length and speed of the wall, respectively. Assuming the system is homogeneous, stationary, and the stress within the sublayer is non-divergent, the corresponding shear stress can be represented as:

$$\tau/\rho_a = u_*^2 = C_D(U - \mathcal{U}_0)^2 \equiv C_D U_r^2 \tag{2}$$

where ρ_a is the air density, u_* is the friction velocity, U and C_D are the airflow and total aerodynamic drag coefficient, respectively, at a fixed height. U_r here is the *air-sea relative wind velocity*. Despite well-recognized limitations, Eqs. (1 and 2) are the basis for physically modeling the dynamics of the lower ABL. This may also be used in empirical studies where the turbulence fluxes are not directly resolved.

Within the terrestrial ABL, it is reasonable to assume $\mathcal{U}_0$ is negligible and $U_r \to U$; however, over water surfaces, this may no longer be the case. In that regime, the air velocity relative to the moving water surface may be significant to quantifying τ. An example of $U_r \neq U$ may be the case of light wind over a channel flow, e.g., river or tidal channel. While this is a physically interesting problem with local significance, these simple cases are insufficient to understand more general, large-scale, geophysical fluid dynamics with applications to weather and climate. To simplify the problem, previous oceanic studies tended to ignore U_r, assuming oceanic currents were much weaker than the wind. Thus, the majority of the previous investigation into τ, and thus C_D, ignored the near-surface hydrodynamics (e.g., Smith and Banke (1975); Smith (1980); Large and Pond (1981); Smith (1988); Yelland and Taylor (1996)). Fairall et al. (2003) was one of the first studies advocating for using the relative wind velocity explicitly. Using the evidence provided by Bigorre et al. (2013), Edson et al. (2013) emphasized Fairall's early argument by explicitly requiring U_r as the input velocity to the widely used bulk flux algorithm, COARE 3.5, in marine atmospheric boundary layer (MABL) studies. The original motivation for this paradigm stemmed from quantifying τ over large-scale ocean currents, e.g., the Gulf Stream, where the surface advection is large and U may be low. This is bolstered and expanded by the satellite- and numerical-based studies showcasing ocean surface current intensity across large swaths of the ocean (Kelly et al. 2001; Dawe and Thompson 2006; Renault et al. 2017). This re-emphasis on the import of U_r has expanded outside of the pure atmosphere-ocean flux community. For example, the hydrodynamic models incorporate U_r explicitly into their free-surface kinematic boundary conditions (Deltares 2020). Despite these conceptual advancements, U_r lacks a rigorous, physics-based definition and is currently applied *ad hoc*.

One of the challenges to defining U_r is characterizing a representative current at the ocean interface. Classically, τ should be applied to a wall moving at some arbitrary speed, $\mathcal{U}_0$. For the case of a solid plate, $\mathcal{U}_0$ is trivially defined as the speed of the plate, however, in the case of a water surface it is less obvious at what velocity are the roughness elements moving. As a first-order approximation, investigators applying the new U_r paradigm to quantifying τ have used a bulk approach:

$$\tau_b = C_D U_{r,b}^2 = C_D(U - \mathcal{U}_b)^2, \tag{3}$$

where $\mathcal{U}_b$ is the mean horizontal current of some upper, near-surface layer. In practice, there is no standard definition of $\mathcal{U}_b$ and it may often be applied without considering the role of vertical current shear on τ. Effectively, the upper ocean surface layer is represented as a rigid slab with a mean advection. This simplification neglects the fundamental complexity of near-surface shear and the interaction these currents have on surface waves (which carry a fraction of the stress) through the Doppler effect. The need to establish a robust, physics-based approach is urgent given recent findings from remote sensing showing significant shear is ubiquitous in the upper ocean (Lund et al. 2020; Laxague et al. 2017, 2018; Morey et al. 2018; Lodise et al. 2019). Furthermore, τ applied to a wavy surface distributes the stress unequally across the spectrum of waves with characteristic wavenumbers k, each with a unique Doppler modulation caused by the shear. Thus, important aspects of the exchange mechanism, especially in the cases where U_r may be important, Eq. (3) cannot adequately capture the relevant physics of vertical current shear and surface waves. In this paper, we present a novel framework where the bulk momentum flux is partitioned into viscous skin and wave form components each applied to their relevant surface advection current. This approach builds on the advancements made by Eq. (3) by entraining our present understanding of stress partitioning and the Doppler modulation of linear surface wavesf. The impact on this framework on bulk air-sea momentum flux quantification will be evaluated through a sensitivity analysis using an extensive oceanic dataset with co-located measurements of direct covariance flux, directional wave spectra, and near-surface current shear.

2 Methodology

2.1 Wind Stress on a Moving Ocean Surface

The stream-wise component of the horizontal momentum balance for an idealized atmospheric boundary layer can be expressed as:

$$\rho_a\left(\frac{\partial U}{\partial t} + U\frac{\partial U}{\partial x} + V\frac{\partial U}{\partial y}\right) = \frac{\partial}{\partial x}\left[-P + 2\mu\left(\frac{\partial U}{\partial x} + \frac{\partial U}{\partial y}\right)\right] + \rho_a\frac{\partial}{\partial z}(-\overline{w'u'}), \tag{4}$$

where [x, y, z] are the right-handed stream-wise, cross-stream, and vertical coordinate, respectively; P is the hydrostatic pressure, the $2\mu(\ldots)$ term is the mean strain rate, and the last term on the right-hand side is the relevant component of Reynolds stress divergence. Here, we have already applied Reynolds decomposition ($x = X + x'$) assuming ergodicity. This balance is greatly simplified if we assume that the system is homogeneous (in the horizontal), stationary, and that we are within an inertial sublayer (Blackadar and Tennekes 1968) such that the impact of viscosity, μ, on the mean flow is negligible. Thus, we find that the Reynolds stress is non-divergent:

$$0 = \rho_a \frac{\partial}{\partial z}(-\overline{w'u'}) \tag{5}$$

$$\frac{\tau_0}{\rho_a} \equiv u_*^2 = \overline{w'u'}, \tag{6}$$

where $\boldsymbol{\tau}_0$ is the wind stress at the surface. Under neutral conditions, there is a well-defined relationship between the mean wind shear and the momentum flux at the surface: (Monin and Obukhov 1954):

$$\frac{\partial U}{\partial z} = \frac{u_*}{\kappa z}, \tag{7}$$

which can be integrated to yield the familiar logarithmic velocity profile:

$$U(z) = \frac{u_*}{\kappa} \ln \left(\frac{z + z_0}{z_0} \right), \tag{8}$$

where z_0 is the surface roughness length and κ is the von Kármán constant. This describes the velocity profile above a stationary, rough boundary; in a general sense, that boundary may be moving with some speed $\mathcal{U}_0$, and thus $U(z) \to U_r \equiv U(z) - \mathcal{U}_0$ (Eq. 1), which may be considered the classic atmospheric boundary layer scenario. The height above the surface where Eq. (6) is valid defines the constant flux (or stress) layer within the atmospheric boundary layer. While this is widely assumed for experimental and numerical purposes, even in an ideal sense a strictly constant flux layer is not essential to the validity of Eq. (8) (Tennekes 1973). Nonetheless, the notion that $\partial \boldsymbol{\tau}_0/\partial z = 0$ is widely assumed, though recent experimental evidence has made a compelling case for this not being generally valid within the atmospheric inertial sublayer (Ortiz-Suslow et al. 2021; Mahrt et al. 2021). For the purposes of developing the present framework, we will assume a constant stress layer exists and discuss the implications of $\partial \boldsymbol{\tau}_0/\partial z \neq 0$ further on.

In early studies of marine boundary layer stress, the limit that $U \gg \mathcal{U}_0$ was widely applied (Smith and Banke 1975; Smith 1980; Large and Pond 1981; Smith 1988; Yelland and Taylor 1996). More recently, Fairall et al. (2003) demonstrated that this assumption was not generalizable, and the authors show the impact this has on parameterizing the aerodynamic drag coefficient for the ocean surface.This was done assuming a rigid slab upper ocean surface layer (Fig. 1a), which simplifies the complexity of accounting for air-sea relative wind. a Thus, the total wind stress at the surface was given as:

$$\boldsymbol{\tau}_0/\rho_a \equiv u_*^2 = C_D(U - \mathcal{U}_b)|U - \mathcal{U}_b|, \tag{9}$$

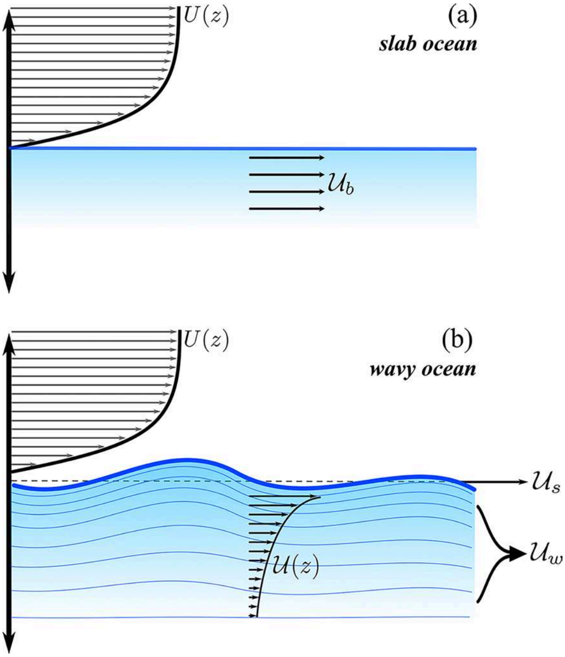

Fig. 1 Conceptual diagram highlighting the distinction between defining the relative wind velocity over the (a) slab ocean versus the (b) wavy interface. In the presence of near-surface shear, the relative contributions of viscous skin ($\mathcal{U}_s$) and wave form ($\mathcal{U}_w$) must be directly accounted when calculating the relative wind at the base of the sheared wind profile

where $\mathcal{U}_b$ is the bulk advection of the slab projected into the mean wind direction ($\mathcal{U}_b = \mathcal{U}_0 cos(\phi)$($\mathcal{U}_0$ is the Eulerian surface current magnitude and ϕ is the relative angle between wind and current). In practice, $\mathcal{U}_b$ is determined opportunistically as a measured (or simulated) current near the surface assuming $\partial \mathcal{U}_b / \partial z \approx 0$. Originally, the argument for defining $\boldsymbol{\tau}_0$ using Eq. (9) stemmed from observations over barotropic ocean currents, e.g., Gulf Stream, with minimal sub-surface shear. However, outside of this domain, there may be non-trivial regimes where $U \sim \mathcal{U}_0$ and $\partial U_s / \partial z \neq 0$, in such cases $\mathcal{U}_b$ would not be suitable. Thus, a more general approach is needed to account for surface advection of the wavy interface (Fig. 1b) in the bulk momentum flux parameterization.

2.2 Bulk Momentum Flux in the Presence of Shear and Waves

The key limitation of the bulk-current approach is that it does not account for the impact of current shear on the waves that carry $\boldsymbol{\tau}_0$. At some distance above the surface, $\boldsymbol{\tau}_0$ may be defined in terms of the Reynolds stress, as in Eq. (6). However, as one approaches the wavy surface, a component of the total stress is caused by flow interactions with the surface undulations. The proportion of this wave form stress, $\boldsymbol{\tau}_w$, to the total stress increases with proximity to the free surface, $\eta(\boldsymbol{x}, t)$. At the interface, $z = \eta$, the total stress may be partitioned into two components (Donelan and Dobson 2001):

$$\boldsymbol{\tau}_0 = \boldsymbol{\tau}_\nu + \boldsymbol{\tau}_w, \tag{10}$$

where $\boldsymbol{\tau}_\nu$ is the viscous component of the stress applied directly to the aqueous ocean skin layer. Outside of very strong wind forcing, $\boldsymbol{\tau}_\nu$ comprises the frictional interaction between airflow and the water mass and is uniformly applied to the ocean surface (Mueller and Veron

2009). The viscous stress component may be parameterized given an assumed smooth airflow Reynolds number (Donelan and Dobson 2001), or using direct measurements over varying wave states from laboratory or (rare) field experiments (Buckley et al. 2025; Veron et al. 2007; Buckley et al. 2020). On the other hand, $\boldsymbol{\tau}_w$ is coherent with the wave phase and is thus applied non-uniformly across the local wave spectrum, $F(\boldsymbol{k})$ over gravity wavenumbers $\boldsymbol{k}$. The proportion $\boldsymbol{\tau}_w/\boldsymbol{\tau}_0$ increases steadily with wind shear and the evolving wave state, and can easily dominate the interfacial momentum transfer (Makin et al. 1995).

Just as $\boldsymbol{\tau}_0$ can be represented using an aerodynamic drag law with a total drag coefficient, C_D, its components may be represented using analogous drag laws and their respective coefficients. This is typical in engineering applications where drag coefficients are used to capture the stress at the wall, where viscous and form (or pressure) drag play a role (Lee et al. 2014, e.g.,). Applying the rationale of Fairall et al. (2003) and Edson et al. (2013), these stress components may be represented as the linear supposition of independent drag laws referenced to their respective mean surface advection currents:

$$\boldsymbol{\tau}_\nu = \rho_a C_{D,\nu}(U - \mathcal{U}_s)|U - \mathcal{U}_s|, \tag{11}$$

$$\boldsymbol{\tau}_w = \rho_a C_{D,w}(U - \mathcal{U}_w)|U - \mathcal{U}_w|, \tag{12}$$

where $\mathcal{U}_s$ and $\mathcal{U}_w$ are the advection currents appropriate to the skin and wave forms, respectively. Putting this together with Eq. (10), the total surface stress takes the form:

$$\boldsymbol{\tau}_0 = \rho_a C_{D,\nu}(U - \mathcal{U}_s)^2 + \rho_a C_{D,w}(U - \mathcal{U}_w)^2, \tag{13}$$

$$\boldsymbol{\tau}_0/\rho_a = C_{D,\nu}(U - \mathcal{U}_s)^2 + C_{D,w}(U - \mathcal{U}_w)^2 = u_*^2. \tag{14}$$

In this formulation, $\mathcal{U}_s$ and $\mathcal{U}_w$ are the ocean skin drift and the mean Doppler current advecting the wave forms, respectively, and $C_{D,\nu}$ and $C_{D,w}$ are the viscous and wave form drag coefficients, respectively. In the absence of shear, $\mathcal{U}_s = \mathcal{U}_w = \mathcal{U}_b$, which can be shown to recover Eq. (9) with $C_D = C_{D,\nu} + C_{D,w}$. Equation (14) presents a bulk drag formulation that explicitly accounts for both the decomposition of the interfacial stress into viscous friction and wave form components, as well as the different components of surface advection that impact each of these stress components. In addressing the complexity of the wavy interface, this approach introduces additional unknowns to the system. The remainder of the manuscript will focus on how to define Eqs. (11 and 12) and the impact this has on $\boldsymbol{\tau}_0$, as compared to the bulk approaches. We assume that u_* is known, and the implications of not knowing it will be discussed below.

2.3 Defining the Forms of $\mathcal{U}_s$ and $\mathcal{U}_w$

We first present our definition for the ocean skin advection, $\mathcal{U}_s$, that appears in Eq. (11). This current is exceedingly difficult to measure in the field, outside of specialized remote sensing techniques (Laxague and Zappa 2020). Within the ocean-side viscous sublayer, the vertical structure of the wind-forced advection should follow the theoretical profile laid out by Prandtl (1910); von Kármán (1939) across the viscous and inertial sublayers. For this analysis, we followed the wall layer coordinate system given by Spalding (1961), which follows the Prandtl-von Kármán models:

$$u_+ = U_d(z)/u_{*,w} \tag{15}$$

$$z_+ = z u_{*,w}/\nu_w, \tag{16}$$

where subscript *w* denotes water-side parameters and U_d is the surface velocity deficit profile: $U_d(z) = \mathcal{U}_s - \mathcal{U}(z)$. The water-side friction velocity is calculated assuming stress continuity at the surface (Wu 1983): $u_{*,w} = u_* \sqrt{\rho_a/\rho_w}$ where ρ_w is the water density. Using Spalding's approach, the expected wind-induced velocity profile is piece-wise:

$$u_+ = \begin{cases} z_+ & z_+ < 5 \\ \frac{2}{\kappa} log(z_+) - 3.05 & 5 <= z_+ < 30 \\ \frac{1}{\kappa} log(z_+) + 5.5 & 30 <= z_+ \end{cases} \tag{17}$$

where the three expressions give the profiles across the viscous laminar, transitional, and inertial sublayers, respectively. The laminar and transition layers span approximately 1-10 mm below the wavy interface. Without a direct measurement of $\mathcal{U}_s$, the *total* skin advection may be extrapolated using the wind-induced shear profile from Eq. (17) (Fig. 2); in the absence of some underlying advection, the wind-induced shear profile provides anindirect estimate of $\mathcal{U}_s$.

We now focus on establishing the wave-form advection surface current, $\mathcal{U}_w$. Over the ocean, the near-surface current may have arbitrary shear, which in some cases can be substantial, and this impact may be described by examining the surface gravity wave dispersion relationship:

$$\Omega(\boldsymbol{k}) = \boldsymbol{k} \cdot \boldsymbol{\mathcal{U}}(k) + \sigma(\boldsymbol{k}), \tag{18}$$

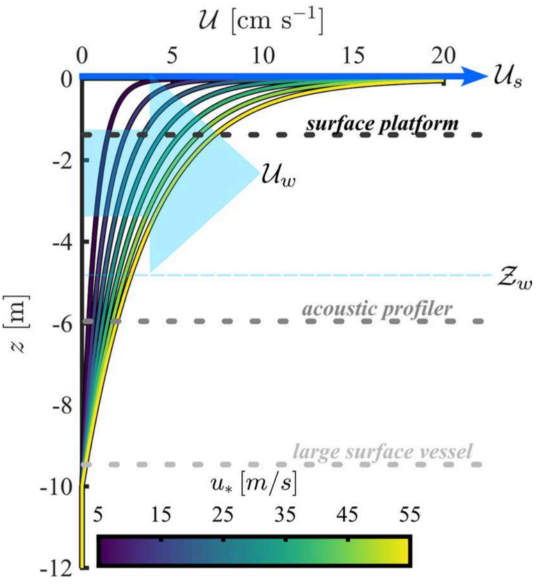

Fig. 2 Idealized wind-induced ocean shear profiles. Conceptual arrows representing $\mathcal{U}_s$ and $\mathcal{U}_w$ are overlaid, where the former will coincide with the surface skin drift and the latter is a weighted average from the depth $\mathcal{Z}_w$ to the surface. The depth of $\mathcal{Z}_w$ varies with the average penetration depth (2k^{-1}) of local waves, hence $\mathcal{Z}_w$ increases with more developed waves. The depths of typical ocean current measurement systems are shown using dashed lines. The depth of "acoustic profiler" is based on an upward-looking system at 50-meters depth, and the depth of the measurement nearest to the surface given known acoustic interference

where the absolute frequency (Ω) includes the Doppler shift, $\boldsymbol{k} \cdot \boldsymbol{\mathcal{U}}(k)$, of the intrinsic wave frequency (σ), and $\boldsymbol{k}$ is the wavevector ($\|\boldsymbol{k}\| \equiv 2\pi/\lambda$, where λ is the surface wavelength). The absolute wave celerity is then $C = \Omega/k$. To define $\mathcal{U}_w$, it is necessary to explicitly connect each $\boldsymbol{k}$ with a corresponding advection current at some depth. In arbitrary water depth, the relationship between $\boldsymbol{\mathcal{U}}(z)$ and $\boldsymbol{\mathcal{U}}(k)$ may be stated as (Kirby and Chen 1989):

$$\boldsymbol{\mathcal{U}}(k) = \frac{2k}{\sinh(2kh)} \int_{-h}^{0} \boldsymbol{\mathcal{U}}(z) \cosh(2k(h+z)) \mathrm{d}z, \tag{19}$$

The above reduces to the form of Stewart and Joy (1974) in deep water. Thus, for a given $\boldsymbol{k}$, the current that satisfies Eq. (18) may be the vertical average of the observed ocean velocity profile over a finite layer with thickness $\mathcal{Z}_w$. This is conceptually depicted in Fig. 2, where $\mathcal{U}_w$ is a $\boldsymbol{k}$-weighted average across a sublayer below the surface. In particular, the depth of $\mathcal{Z}_w$ is expected to be inversely proportional to the $\boldsymbol{k}$ at the peak of the wave energy spectrum. Several empirical solutions for defining $\mathcal{Z}_w$ have been proposed. The conventional approach has been to assume a functional form (e.g., linear, exponential, etc.) of the near-surface shear and estimate $\mathcal{Z}_w$ as some fraction of λ (Stewart and Joy 1974; Plant and Wright 1980). Direct iterative approaches have been proposed that arrive at $\mathcal{Z}_w$ for an arbitrary $\mathcal{U}(z)$ (Campana et al. 2016; Smeltzer et al. 2019). Regardless of the methodology, Eq. (19) quantifies $\boldsymbol{\mathcal{U}}(k)$ for all $\boldsymbol{k}$ across a finite depth $\mathcal{Z}_w$.

Equation (19) links the current shear to the waves across the spectrum of $\boldsymbol{k}$. However, Eq. (12) requires a mean wave form advection current, $\mathcal{U}_w$. The portion of the surface stress carried by the waves has been referred to as the wave form stress, $\boldsymbol{\tau}_w$. This is analogous to the form drag in the case of a static surface at the base of a wall flow. The resulting $\boldsymbol{\tau}_w$ is the integration of each $\boldsymbol{k}$ contribution to the wave form stress:

$$\boldsymbol{\tau}_w \equiv \int_{\boldsymbol{k}} \boldsymbol{\tau}_{w,k}(\boldsymbol{k}) \mathrm{d}\boldsymbol{k}, \tag{20}$$

where $\boldsymbol{\tau}_{w,k}(\boldsymbol{k})$ is the form stress spectral density. This may be represented in terms of wave energy input from the wind, S_{in} (Jones et al. 2001),

$$\boldsymbol{\tau}_w = \rho_w g \int_{\boldsymbol{k}} \frac{S_{in}(\boldsymbol{k})}{c_0} F(\boldsymbol{k}), \tag{21}$$

$$= \alpha \rho_w g \int_{\boldsymbol{k}} \left(\frac{u_*}{c_0}\right)^2 \cos(\theta) \boldsymbol{k} F(\boldsymbol{k}) \mathrm{d}\boldsymbol{k}, \tag{22}$$

where Eq. (22) follows Plant (1982) assuming the the wavenumber-directional spectrum and $\boldsymbol{\tau}_0/\rho_a = u_*^2$ is known. Here, g is the gravitational acceleration, c_0 is the intrinsic phase speed, θ is the relative wind–wave angle, $F(\boldsymbol{k})$ is the surface elevation variance density spectrum, and α is an empirical parameter (determined from the laboratory to be 0.04 ± 0.02). Equation 20 defines $\boldsymbol{\tau}_w$ across all $\boldsymbol{k}$, and Eq. (22) provides a means of estimating this from wind and wave parameters; however, not all $\boldsymbol{k}$ contribute *equally* to the $\boldsymbol{\tau}_w$ and, hence, $\boldsymbol{\tau}_0$. As in the wave-current modulation governed by a Doppler term, $\boldsymbol{k} \cdot \boldsymbol{\mathcal{U}}(k)$, the amount of stress carried by the waves is proportional to $\boldsymbol{k}$. Thus, we define the mean wave-form advection current as the current of encounter for all $\boldsymbol{k}$, weighted by their contributions to $\boldsymbol{\tau}_0$:

$$\mathcal{U}_w = \frac{1}{\tau_w} \int \boldsymbol{\tau}_{w,k}(\boldsymbol{k}) \cdot \boldsymbol{\mathcal{U}}(k) \, \mathrm{d}\boldsymbol{k}, \tag{23}$$

In practice, the integrand should be defined across the gravity wave band, nominally for $|k| < 100$. In the case of young waves, $U \gg c_0$, $\boldsymbol{\tau}_w$ is carried predominantly by short, steep waves that are impacted by the near-surface currents. Thus, $\mathcal{Z}_w$ tends to shallow due to $\boldsymbol{k} \cdot \boldsymbol{\mathcal{U}}(k)$ being dominated by large $\boldsymbol{k}$. In the case of $U < c_0$, $\boldsymbol{\tau}_w$ is distributed across a larger range of $\boldsymbol{k}$ and the contributions of longer waves deepen $\mathcal{Z}_w$ and decrease the average $\boldsymbol{k} \cdot \boldsymbol{\mathcal{U}}(k)$. This effectively decreases $\mathcal{U}_w$ as the mean wave form advection moves further down the sheared profile.

2.4 Evaluating this Framework Using an Observational Dataset

In the sections above, we presented a physical framework to defining the air-sea drag which builds on the notion of stress partitioning at the air-water interface into viscous skin and form stress components. This framework also accounts for the relative motion between the surface and the airflow using the mean surface advection relevant to the ocean skin and wave forms. In order to quantify this framework's effects (e.g., as compared to the conventional approach of Eq. (2), we have applied it to a field observational dataset. The Ocean Observatories Initiative (OOI) provides public access to the turbulent momentum flux, directional wave spectra, and current profile information required for applying our framework. We utilized a dataset collected over the course of seven years (2017–2023) from the Oregon Shelf Mooring (CE02SHSM) at OOI's Coastal Endurance Array. The mooring is comprised of a surface float, sub-surface in-line sensor frame, and a bottom mounted node to collect comprehensive biogeochemical and physical oceanographic data. For complete details, the reader is directed to https://oceanobservatories.org/site/ce02shsm/, the relevant information for this study will be discussed here.

CE02SHSM is in 80 m of water approximately 18 km west of Newport, Oregon (Fig. 3). There are several distinct advantages to using these data for this analysis: (1) the range of the dataset goes back seven years with good temporal coverage, (2) there are co-located wind, wave, and current measurements at hourly intervals for in-depth analysis, and (3) the site is exposed to a wide range of wind, wave, and current conditions (Fig. 4). Furthermore, by using this dataset, we take advantage of internal quality data control and processing steps that are standardized across the OOI array network. The wind and stress measurements stem from the Direct Covariance Flux, High Power (FDCHP) system which is owned and operated by the Woods Hole Oceanographic Institution. These data are provided hourly from 20-minute covariance calculations of the Reynolds stress, amongst other parameters. Data are processed following methods laid out by Edson et al. (1998) and complete details may be found at https://oceanobservatories.org/instrument-class/fdchp/. The key measurement stems from the omnidirectional Gill R3 ultrasonic anemometer-thermometer. Water surface elevations are reconstructed from a six degree-of-freedom motion system and integrated magnetometer, from which the onboard TRIAXYS directional wave sensor computes directional wave spectra over 30-minute discrete windows and reported on an hourly basis (see

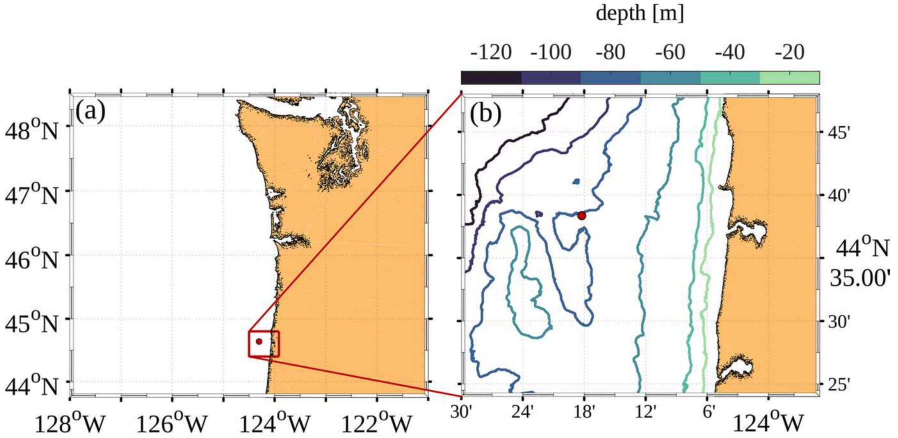

Fig. 3 **a** Map of Pacific Northwest of the United States and **b** focusing on the Oregon portion of the OOI Coastal Endurance array, with the Oregon Shelf mooring (CE02SHSM) marked as a red dot (44.6393° N, 124.3040° W); bathymetry data taken from NOAA (2003)

https://oceanobservatories.org/instrument-class/wavss/ for details). For this system, the reported frequency vector is 0.005–0.64 Hz discretized across 128 bins; however, we truncated the spectra at a high frequency cutoff f_c of 0.35 Hz. Directional wave information is estimated using maximum entropy method with 121 directional bins from [0°, 360°]. The current profile was constructed from two sources: (1) a bottom-mounted acoustic Doppler current profiler (600 kHz RDI Workhorse) with a nominal depth range of 80–10 m and (2) a near-surface acoustic Doppler current profiler (Nortek Aquadopp 300 m) mounted at 1 m depth on the surface float and used as a single-point velocimeter. A moving 5-sample median filter was applied to the current data before re-sampling onto the hourly time basis of the wind and wave measurements. The coalesced dataset used in our analysis contains approximately 13,000 hourly co-located samples of wind speed, wind stress, the current velocity profile, and the directional wave spectrum.

The wavevector $\boldsymbol{k}$ and wavenumber-directional spectrum $F(\mathrm{k})$ are ubiquitous in our framework. However, the TRIAXYS directional wave sensor provides only the frequency-directional spectrum $F(\Omega, \theta)$. In order to obtain $\boldsymbol{k}$, we inverted the Doppler shift (Eq. 18) given our observed absolute wave radian frequency Ω and direction θ. This was accomplished through pre-allocation of a high-resolution synthetic array of $\omega(k)$ obeying the linear dispersion relation. The absolute frequency Ω was then computed for each possible wave direction in response to the directional advection current $\boldsymbol{\mathcal{U}}(k)$. The wavenumber corresponding to each frequency bin was then selected by minimizing the difference between observed and synthetic values of Ω. Finally, the wavenumber-directional spectrum $F(\mathrm{k})$ was computed by requiring that wave elevation variance be conserved during coordinate transformation (Plant 2009):

$$\int_{-\pi}^{+\pi}\int_{0}^{\infty} F(k,\theta) k \mathrm{d}k \mathrm{d}\theta = \int_{-\pi}^{+\pi}\int_{0}^{\infty} F(\Omega,\theta) \mathrm{d}\Omega \mathrm{d}\theta, \tag{24}$$

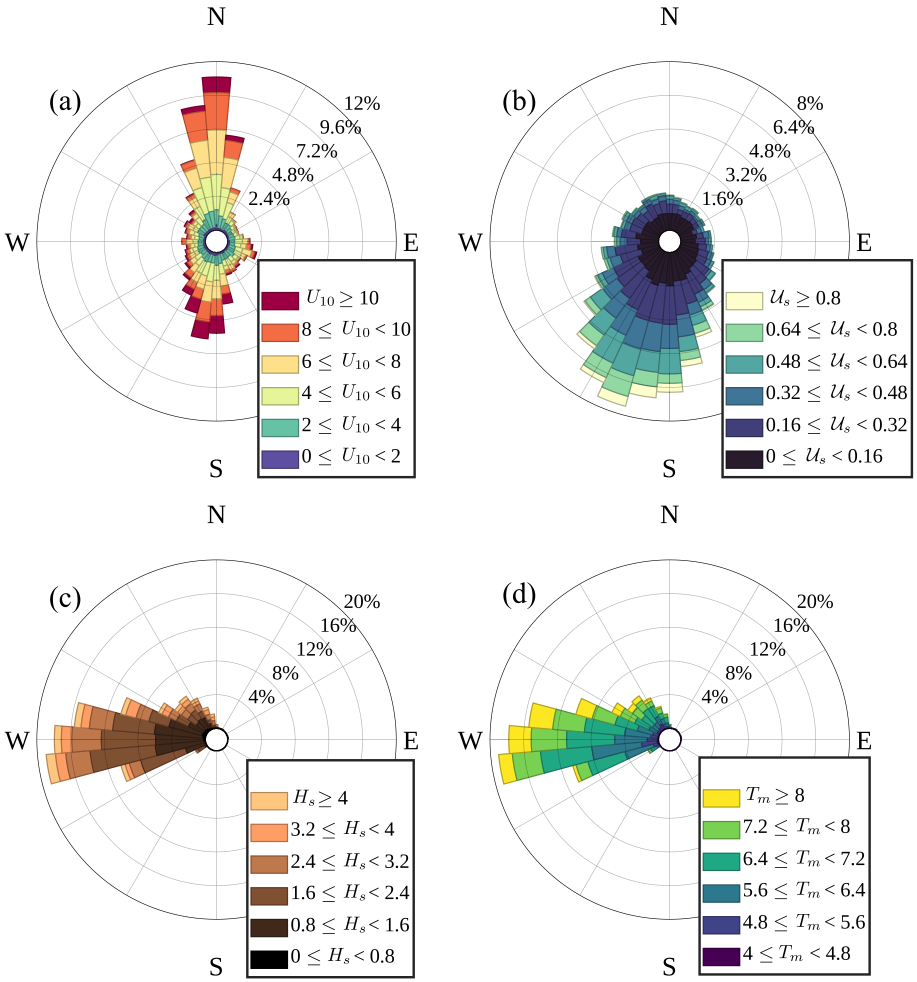

Fig. 4 Direction/magnitude histograms in meteorological ("coming-from") convention: **a**U_{10}, the ten-meter wind speed in m s^{-1}; **b**U_S, current magnitude at ≈1.5 m depth in m s^{-1}; **c**H_s, significant wave height in m; **d**T_m, mean wave period (to be specific– T_{m02}) in s

from which it follows that

$$F(k, \theta) = \frac{C_g}{k} F(\Omega, \theta), \tag{25}$$

where C_g is the absolute group speed $\partial\Omega/\partial k$. Our high frequency cutoff f_c corresponds to a wavenumber of approximately 0.5 rad m^{-1} in the absence of current. In order to extend our wave spectra deeper into the short gravity wave regime, we performed a directionally-varying wave spectral tail extrapolation out to $k_{high} = 50$ rad m^{-1}: each dimensionless spreading function $D(k, \theta) \equiv F(k, \theta)/F(k)$ was linearly interpolated on $k \in [0.5, 50]$ rad m^{-1}, while each omnidirectional wavenumber spectrum $F(k)$ was augmented with a piece-wise power-law tail, transitioning from $k^{-2.5}$ to k^{-3} at the wavenumber corresponding to a pre-determined degree of saturation:

$$F(k) \propto \begin{cases} k^{-2.5}, & k^3F(k) = B(k) < 8 \cdot 10^{-3} \\ k^{-3}, & k^3F(k) = B(k) \geq 8 \cdot 10^{-3} \end{cases} \tag{26}$$

The value chosen for this critical degree of saturation $B_{sat} \approx 8 \cdot 10^{-3}$ was informed by (Lenain and Melville 2017) and is consistent with classically-obtained values for the quantity (Phillips 1985, e.g.). The coefficient (vertical level in log-space) was selected to minimize spectral energy difference across overlapping wavenumbers between the tail and the observational spectrum.

3 Results

Here, we demonstrate the framework of Eq. (14) using oceanic buoy data where direct covariance stress, directional wave spectra, and surface currents were simultaneously measured for a multi-year record. The OOI data record for this site spans (spring) 2017 through 2023, with some gaps during the 2020 year caused by COVID interruptions to platform services. This is an energetic region characterized by strong wind and waves throughout the year, especially during the boreal winter. The wind was predominantly from the north, with substantial portions of southerly wind vectors (Fig. 4a). The wind was orthogonal to the predominant westerly wave systems in the region, leading to a highly mixed sea state environment (Fig. 4c, d). The median wind speed was approximately 6 m s^{-1}, but with an interdecile (10^{th}–90^{th} percentile) range spanning 3–10 m s^{-1} (Fig. 5a). The median significant wave height, H_s, was 2 m, with an interdecile range spanning a little over 1 to just under 4 m (Fig. 5c); the mean wave period spanned 5–15 s, with a median of 8 s (Fig. 5d). The surface currents, $\mathcal{U}_s$, tended be from the south (Fig. 4b) with a median speed of 0.25 m s^{-1} (or 4% of U_{10}), although $\mathcal{U}_s$ above 0.5 m s^{-1} were common (Fig. 5b).

Figure 6 examines variability of the derived $\mathcal{U}_s$ with observed 10-m equivalent wind speed, U_{10}. $\mathcal{U}_s$ was estimated by extrapolating the sub-surface current measurements from the acoustic sensors and Eq. (17). Conventionally, the surface skin advection is expected to be approximately 3% of the mean wind speed (Wu 1975), or 53% of the air-side friction velocity (Wu 1983). From the OOI analysis, these thresholds tend to underestimate the parameterized surface current, especially at low U_{10}. Furthermore, the overall trend in $\mathcal{U}_s$ is more complex than can be represented by these fixed values. For instance, at $U_{10} <$ 4 m s^{-1}, $\mathcal{U}_s$ was more than 33% higher the conventional threshold. In a mean sense, the observation-derived $\mathcal{U}_s$ tended to converge on Wu (1975) 3% value, but there is a suggestion that this underestimates surface currents beyond 10 ms^{-1}. Relative to the friction velocity, the observed $\mathcal{U}_s$ was significantly higher than the expected $0.53u_*$ across the entire observational range of mean winds, however the observed $\mathcal{U}_s/u_*$ tended to decrease, suggesting that it would approach the expected value at larger U_{10}.

The implications of Eqs. (10 and 14) is that the total stress at the interface is comprised of multiple components, each with their own respective surface advection. In general, we expect the viscous skin stress to dominate at low U (and in the absence of waves), and the wave form stress to progressively increase as surface waves develop. Figure 7 examines this

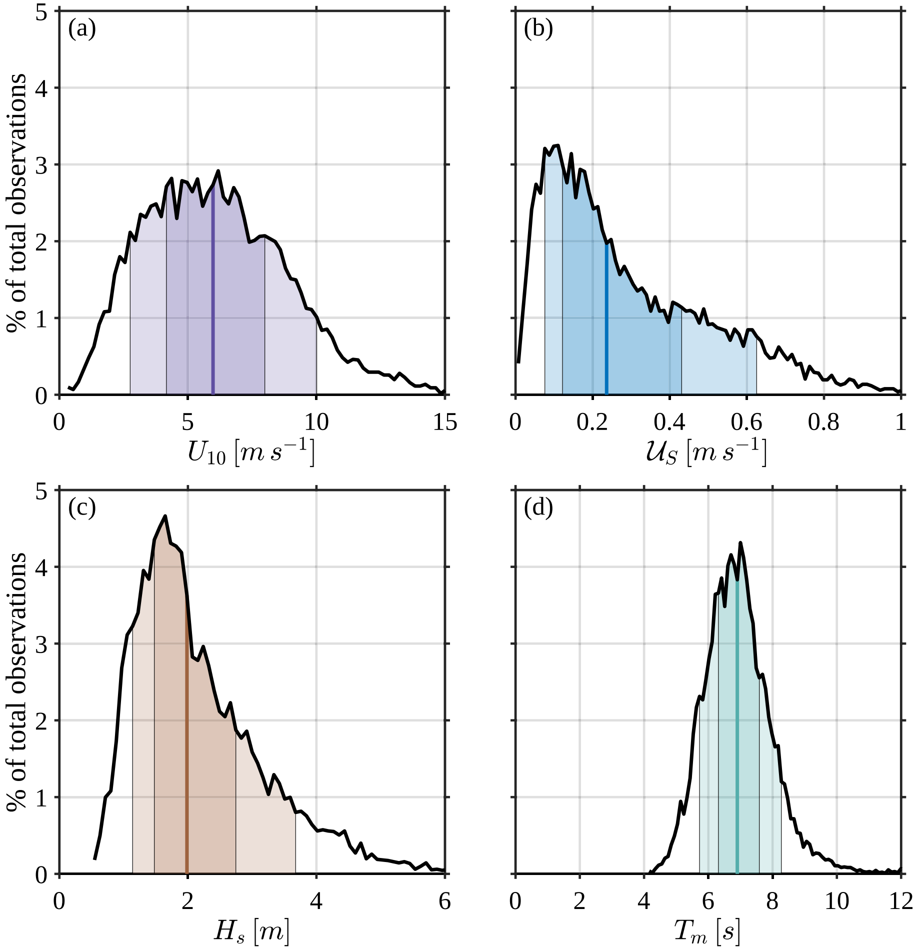

Fig. 5 Probability density functions for **a**U_{10}, **b**$\mathcal{U}_S$, **c**H_s, and **d**T_m. Light region indicates interdecile range, dark region indicates interquartile range, and thick colored segment indicates the 50^{th} percentile

stress budget in a frame agnostic of surface currents (i.e, no current information), applying a bulk, or slab, current (i.e., no upper ocean shear), and a full sheared current profile using the extrapolation methods discussed above. For completeness, we have introduced τ_{br} in Fig. 7 following the model given by Mueller and Veron (2009)– a framework which we have integrated here to account for physical processes such as feedbacks associated with airflow separation and the reduction in wave growth rate with increasing wave age. As expected, accounting for currents, sheared or otherwise, does not impact the overall dependence of $\tau_{x/\boldsymbol{\tau}_0}$ with wind speed. However, including current information does exert some noteworthy influence on the distribution of stress across different components. In particular, currents tend to decrease the contribution of $\boldsymbol{\tau}_\nu$ to the overall stress in favor of $\boldsymbol{\tau}_w$ (and τ_b) through wave-current interaction. Further re-distribution of stress to the wave components occurs when accounting for current shear as (1) $\mathcal{U}_s$ is systematically underestimated in a slab approach and (2) the modulation of the wave field is not uniform across $\boldsymbol{k}$. The impact

Fig. 6 $\mathcal{U}_s$ parameterized from field observations following velocity defect approach and assuming negligible background flow, represented as **a** percentage of ten-meter wind speed and **b** fraction of of air-side friction velocity. Dashed lines indicate canonical values provided by (**a**) Wu (1975) and (**b**) Wu (1983). Observations have been bin-averaged using 12 discrete, uniform bins (1102 sample points per bin) with shading across the interquartile range

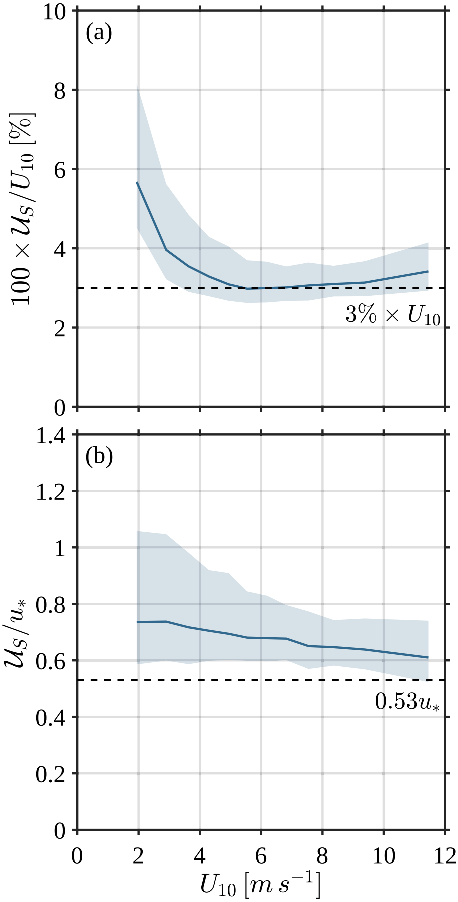

Fig. 7 Decomposition of the various stress magnitudes, in the style of Mueller and Veron (2009), for the different current regimes tested in this study and across the entire OOI dataset analyzed here. Above, $\mathcal{U}_i$ is the surface advection, $\mathcal{U}_s$ and $\mathcal{U}_w$, respectively, corresponding to the appropriate stress component. $\mathcal{U}_w$ was used for the breaking stress magnitude τ_{br}

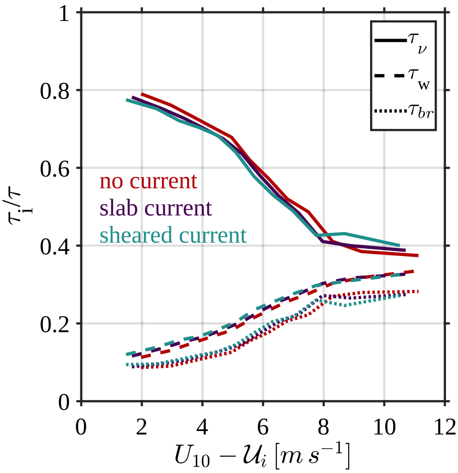

of currents on the stress budget was observed consistently throughout the range of U_{10} with some suggestion of a flip in the sign of the effect on $\boldsymbol{\tau}_\nu$. However, we could not definitively confirm this given the limited data range.

The typical parametric formula for $\boldsymbol{\tau}_0$ hinges on the sea state- and height-dependent drag coefficient, C_D. In a similar vein to U_{10}, the drag coefficient is typically defined as the 10-m value transformed to neutral thermal stratification. By partitioning the stress (Eq. 10), we have introduced two independent drag coefficients, $C_{D,\nu}$ & $C_{D,w}$, each defined using the same 10-m neutral convention (Fig. 8). Similar to the stress budget analysis, we do not expect the introduction of currents, sheared or otherwise, to dramatically impact the overall dependence of $C_{D,i}$ on the wind speed, e.g., Fig. 8a and b. Here, the total dataset has been filtered using discrete *relative* wind speed bins 2 ms^{-1} wide; in the figure, the trend line marks the bin-wise median and the shading spans the interquartile range, or the middle 50%

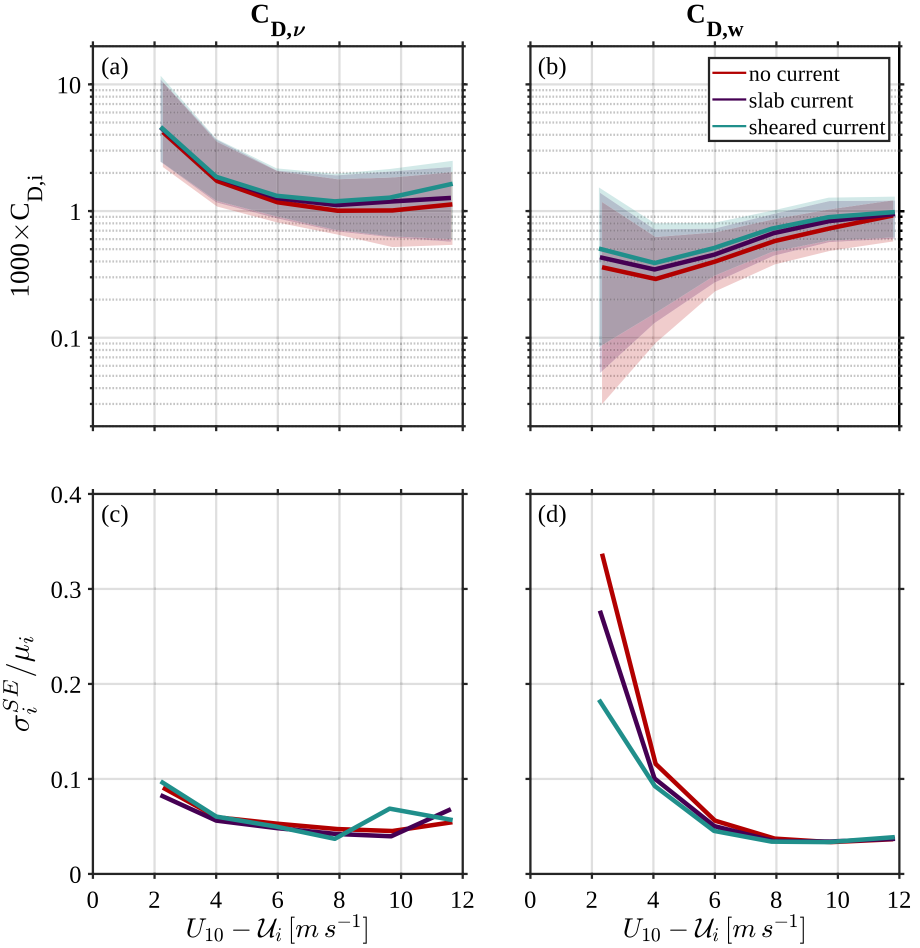

Fig. 8 Dependence of **a** viscous and **b** wave form drag coefficients as a function of their respective relative wind speeds. The shading spans the interquartile range (25^{th}-75^{th} percentile) about the median (solid line). The full dataset has been filtered using a *relative* wind speed 2 ms^{-1} wide discrete bin. (**c**, **d**) Give the relative uncertainty, σ_i^{SE}/μ_i, or the ratio of the standard error to the mean per wind speed bin, for the i^{th} current regime tested in this analysis for the viscous and wave form drag coefficients, respectively.

of derived drag coefficient estimates. The effect that currents (and wave-current interaction) have on the variability of the drag coefficients was analyzed using the relative standard error per wind speed bin, σ_i^{SE}/μ_i, where i refers to the mode: no current, slab current, and sheared current, and μ is the bin-wise average. Overall, for $C_{D,\nu}$, there was neither a discernible effect of currents on the wind speed trend, nor on the drag variability (Fig. 8c). For $U_{10} > 8 - 10\mathrm{ms}^{-1}$ there was some divergence in the medians across the three current regimes, suggesting that using a sheared current profile may tend to increase $C_{D,\nu}$, relative to the slab and no current scenarios. This also coincided with relatively increased variability in $C_{D,\nu}$ at these wind speed ranges.

For $C_{D,w}$, however, the results differed significantly. The effect of currents was evidenced through an offset across almost the entire wind speed range tested in this analysis (Fig. 8b), but at the highest wind speed bin all trends converged. For instance, from 2 to 5 ms^{-1}, $C_{D,w}$ derived using current shear was 17–20% higher than a current-agnostic approach. During this span, the wave form stress ($\boldsymbol{\tau}_w$) comprises 10–20% of $\boldsymbol{\tau}_0$. This offset in the median $C_{D,w}$ remains above 5% until ≈10 ms^{-1}, whereby $\boldsymbol{\tau}_w$ comprises 20–35% of the total stress. The largest effect was on the relative variability in $C_{D,w}$ (Fig. 8d). Below 3 ms^{-1}, the variability in the current agnostic $C_{D,w}$ was 40–50% higher than the drag coefficient derived using a sheared profile. This reduction in relative uncertainty remains above 10% until 9 ms^{-1}, by which point all three modes have a relative uncertainty below 5% of the bin-wise mean.

Following Fig. 7, we examine the the relative impact on the total and component-wise stress, excluding τ_b (Fig. 9). For this, we define $\hat{\tau}_i$ as the mean stress, per current regime i, normalized by the equivalent value using the full current profile, i.e.,with shear, which by definition makes $\hat{\tau}_{sheared\,current} \equiv 1$. In Fig. 9, the shading spans the 95% confidence interval, which has also been normalized by mean stress calculated using the shear profile to make it appear on the same axis. In general, there are significant differences in the estimated stress components ($\boldsymbol{\tau}_\nu$,$\boldsymbol{\tau}_w$) and resulting total stress ($\boldsymbol{\tau}_0$) when considering no, slab, and sheared current profiles (see summary in Table 1). As expected, alternative stress distributions differed the most at the lowest relative wind speeds, but were non-trivial and statistically significant for higher winds. Specifically, *not* including current information lead to nearly 20–50% *overestimation* of $\boldsymbol{\tau}_0$ for relative winds below 5 ms^{-1}, as compared to the

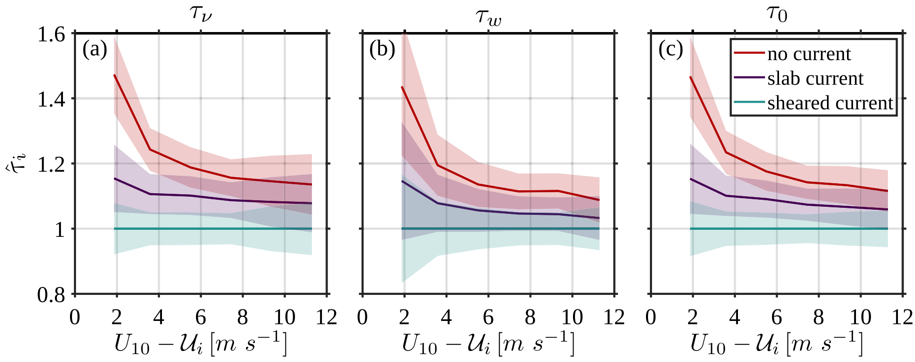

Fig. 9 The median stress (shading spans $\pm 1.96\sigma^{SE}$) for the viscous (**a**), wave form (**b**), and total (**c**) stress, where each has been normalized by value using a sheared current profile. This relative stress, per current regime tested here, is denoted $\hat{\tau}_i$

Table 1 Mean relative differences of between the no current (*no*), slab ocean (*slab*), and full sheared profile (*shear*) regimes tested in this analysis

$U_{10} - \mathcal{U}_i$	N	$\frac{\tau_0^{no} - \tau_0^{shear}}{\tau_0^{shear}}$	$\frac{\tau_0^{slab} - \tau_0^{shear}}{\tau_0^{slab}}$	$\frac{\tau_0^{no} - \tau_0^{slab}}{\tau_0^{slab}}$
1.86	1015	0.468**	0.153*	0.273**
3.58	2902	0.234**	0.101*	0.121**
5.51	3412	0.175**	0.091*	0.078*
7.44	2886	0.142**	0.074*	0.064
9.33	1564	0.133**	0.067	0.063
11.3	456	0.116*	0.059	0.053

This comparison corresponds to the curves in Fig. 9c. A two-sided Student's t-test was used to determine each difference's significance, * denotes cases where $p < 0.05$, ** denotes $p < 0.005$

stress calculated using a sheared profile. Similar scale differences were found for the individual stress components as well. Furthermore, the relative differences remained above 10% up to $\sim$11 ms^{-1}. These differences were all significant to the 95% confidence level. Except for relative wind above $\sim$9 ms^{-1}, significant differences were found when comparing stress calculated using a slab versus sheared current profile. However, these differences were less sensitive to increasing wind, varying between 5 and 15% net difference.

4 Discussion

One of the challenges to demonstrating the framework presented in this study—as summarized by Eq. (14)—is finding a suitable empirical dataset. The Coastal Endurance Array OOI field dataset was essential for the sensitivity tests we performed here. OOI datasets offer significant advantages for such process studies, foremost of which is the measurement of the eddy (direct) covariance momentum flux. A limitation of OOI datasets lie in their measurement of the near-surface current profile; we reconstructed a profile from disparate acoustic sensors and parameterized wind drift on top of that profile (Eq. 17). Although more robust measurements of $\mathcal{U}(z)$ using more advanced experimental techniques would have improved the analysis, the approach used here was sufficient to demonstrate the effect size of our framework.

Sub-meter length waves are of outsize importance for mediating air-sea momentum flux–and these short waves are particularly sensitive to the velocities in the uppermost decimeter of the water column. Therefore, a key aspect of this project involved appropriately parameterizing the wind-induced surface drift as part of the mean surface skin advection $\mathcal{U}_s$. Conventional definitions that are based on wind speed—or opportunistically defining a bulk near-surface current, $\mathcal{U}_b$, in the absence of shear—may significantly misrepresent $\mathcal{U}_s$ in relatively low winds, i.e., below 5 ms^{-1} (Fig. 6). As expected, under this regime, we found that accounting for surface advection had the strongest impact on the derived drag coefficient and momentum flux; however, significant, non-trivial differences persisted into the moderate relative wind speeds included in this analysis. The low subrange of wind speeds tends to be a domain with heightened air-sea flux uncertainty, for a myriad of reasons. In part, this regime may shift from shear to buoyancy driven turbulence which leads to non-stationarity and vertical flux divergence. Furthermore, in low winds there may be measurement uncertainty from sensor noise and/or sample contamination. While our framework cannot directly address these aspects explicitly, we are able to show a significant reduction in drag uncertainty (for $C_{D,w}$) at relative low winds that is directly associated with accounting for wave-current interaction over sheared surface currents (Fig. 8d). This suggests that our framework may help to constrain uncertainty in air-sea momentum flux associated with wind-wave-current interaction and lingering spread in experimental findings may be attributable to other processes (non-stationarity, divergence, etc.) that might be addressed through other means. Further study is needed to understand the effect this has on the scalar heat and gas fluxes, which are stimulated by the momentum flux, and atmosphere-ocean coupled dynamics at larger scales.

The crux of the physical framework described here hinges on the partitioning of surface wind stress at the interface into viscous and wave form components, forcings that are applied to different aspects of the *total* surface advection. While we argue this provides a more physically robust approach to momentum flux quantification across the interface, the cost is paid by the additional empirical terms to the system, e.g., Eq. (14). Furthermore, in the absence of a complete datasets, e.g., near-surface current profile, wavenumber-frequency spectrum, etc., additional parameterizations were used to provide closure. This approach is typical of numerical prediction systems where direct integration of the physics is not computationally feasible. In some cases, the need to entrain further parameterized terms may seem unnecessary. However, as demonstrated using the OOI dataset, the advantage of using these additional terms is a significant reduction in drag uncertainty and systematic changes to the mean total momentum flux at the air-sea interface. Due to limits on the OOI dataset, our analysis does rely on some empirical relationships that are widely used in the literature under similar contexts. For example, our approach to quantifying $\boldsymbol{\tau}_w$ relies on a specific form of S_{in} (Plant 1982), which was chosen based on the information available from the test dataset. In other analysis conducted as part of this study (not shown here), alternative input functions have been tested, (e.g., in the style of Snyder et al. 1981; Jeffreys 1925). While some sensitivity to S_{in} was found, the overall findings of this analysis did not change. Furthermore, the physical framework presented here is agnostic to these individual choices of parameterization.

The focus of this study has been on the low to moderate wind regime. While Fig. 7 does include τ_b, we do not directly investigate the dynamics under stronger forcing where wave breaking is expected to play a more substantial role. In this regime, we expect the air-sea relative wind to have diminishing importance, however the advent of significant breaking and the role this has on the viscous skin and wave form drag remains under explored outside of laboratory or theoretical studies. More developments are needed to generalize our framework to strong forcing conditions. As a final note, our analysis used buoy-derived wave frequency-directional spectra. Future experimental work should prioritize co-located measurement of the three dimensional wavenumber frequency spectrum, $F(\boldsymbol{k}, \omega)$ to allow for directly extracting the current information from the full dispersion relationship. Methodologies using radar- and optical-based remote sensing have been demonstrated to be effective, but they are not typical to experimental datasets. Further advances in this area will improve the use of our approach in future studies. Our approach for defining $\mathcal{U}_s$ may neglect the Eulerian mean wave-induced advection by the orbital motions; further understanding of how to best incorporate this contribution into the overall framework will be the focus of future work.

5 Conclusions

The aim of this study is to develop a physics-based approach to bulk air-sea momentum flux that accounts for the role of upper-ocean current shear and surface waves. This work hinges on the concept of interfacial stress partitioning into viscous skin and wave form components which can be parameterized using aerodynamic drag laws. The role of vertical current shear is included through applying each stress component in a reference frame moving with the surface advection relevant to the contribution to the total stress on the interface. The appropriate surface current for the viscous skin stress is the mean advection of the aqueous skin layer, which we extrapolated using the inertial wall layer formulations. The appropriate current for the wave form stress is the mean current of encounter acting on the wave field through Doppler modulation. This approach accounts for the non-uniform distribution of stress across the wave spectrum, which is weighted toward high $\boldsymbol{k}$, whose Doppler shift is expected to be stronger as predicted by linear dispersion. We tested the framework using a 7-year time series of direct covariance wind stress, directional wave spectra, and upper-ocean current profiles from an OOI buoy platform in the Coastal Endurance Array. In general, our framework does not modify the overall dependence of $\boldsymbol{\tau}_0$, or C_D, on wind speed, but it significantly reduces the overall uncertainty, especially for winds below 4 ms^{-1}. In this case, the wave form drag variability was reduced by 40–50% if accounting for the vertical current shear as compared to shear-free, or slab ocean, bulk current. Furthermore, at wind speeds below 5 ms^{-1}, our approach accounted for a systematic overestimation of $\boldsymbol{\tau}_0$ by nearly 20–50%, if neglecting current information. Simply including a slab ocean equivalent bulk current cannot account for this systematic bias in $\boldsymbol{\tau}_0$ due to missing the nonlinear role of wave-current interaction. Further effort is needed to understand the implications of this framework in numerical simulation with large spatio-temporal integrations and with the advent of wave breaking which further redistributes the incident atmospheric stress onto the ocean surface.

Acknowledgements This material is based upon work supported by the Ocean Observatories Initiative (OOI), a major facility fully funded by the National Science Foundation under Cooperative Agreement No. 1743430, and the Woods Hole Oceanographic Institution OOI Program Office. The authors are grateful to the insight and constructive comments on an earlier version of this study from Profs. Brian Haus and Qing Wang. DOS was supported by the Office of Naval Research Young Investigator Program through grant N0001424WX01687; NL was supported by NSF Award 23-40712; MC was partly supported by the ONR grants N000142012102 (Coastal Land Air-Sea Interaction DRI) and N000142412598 (in collaboration with the Study on Air-Sea Coupling with WAves, Turbulence, and Clouds at High winds MURI). All of the codes used to generate the graphics shown in this manuscript—and the scripts and functions which produced the constituent products given OOI and NDBC data—are available at https://github.com/unh-cassll/waves-currentshear-windstress.

References

Bigorre SP, Weller RA, Edson JB et al (2013) A surface mooring for air-sea interaction research in the gulf stream. Part II: analysis of the observations and their accuracies. J Atmos Ocean Technol 30(3):450–469. https://doi.org/10.1175/JTECH-D-12-00078.1

Blackadar AK, Tennekes H (1968) Asymptotic similarity in neutral barotropic planetary boundary layers. J Atmos Sci 25:1015–1020

Buckley MP, Horstmann J, Savelyev I et al (2025) Direct observations of airflow separation over ocean surface waves. Nat Commun 16:5526. https://doi.org/10.1038/s41467-025-61133-1

Buckley MP, Veron F, Yousefi K (2020) Surface viscous stress over wind-driven waves with intermittent airflow separation. J Fluid Mech 905:31. https://doi.org/10.1017/jfm.2020.760

Campana J, Terrill EJ, de Paolo T (2016) The development of an inversion technique to extract vertical current profiles from X-band radar observations. J Atmos Oceanic Tech 33(9):2015–2028. https://doi.org/10.1175/JTECH-D-15-0145.1

Dawe JT, Thompson L (2006) Effect of ocean surface currents on wind stress, heat flux, and wind power input to the ocean. Geophys Res Lett 33(L09):604. https://doi.org/10.1029/2006GL025784

Deltares, (2020) Delft3D Flexible Mesh Suite. Tech. rep, Deltares

Donelan M, Dobson FW (2001) The influence of swell on the drag. In: Jones IS, Toba Y (eds) Wind stress over ocean, 1st edn. Cambridge University Press, New York, pp 181–189

Edson JB, Hinton AA, Prada KE et al (1998) Direct Covariance Flux Estimates from Mobile Platforms at Sea*. J Atmos Ocean Technol 15(2):547–562.

Edson JB, Jampana V, Weller RA et al (2013) On the exchange of momentum over the open ocean. J Phys Oceanogr 43(8):22. https://doi.org/10.1175/jpo-d-12-0173.1

Fairall CW, Bradley EF, Hare JE et al (2003) Bulk parameterization of air-sea fluxes: updates and verification for the COARE algorithm. J Clim 16:571–591

Jeffreys H (1925) On the formation of water waves by wind on the formation of water waves by wind. Proc R Soc Lond Ser A 107(742):189–206

Jones IS, Volkov YA, Toba Y et al (2001) Overview. In: Jones IS, Toba Y (eds) Wind Stress Over Ocean, 1st edn. Cambridge University Press, Cambridge, p 307

Kelly KA, Dickinson S, McPhaden MJ et al (2001) Ocean currents evident in satellite wind data. Geophys Res Lett 28:2469–2472. https://doi.org/10.1029/2000GL012610

Kirby JT, Chen TM (1989) Surface waves on vertically sheared flows: approximate dispersion relations. J Geophys Res Oceans 94(C1):1013–1027. https://doi.org/10.1029/JC094iC01p01013

Large W, Pond S (1981) Open ocean momentum flux measurements in moderate to strong winds. J Phys Oceanogr 11:13

Laxague N, Haus B, Ortiz-Suslow D et al (2017) Passive optical sensing of the near-surface wind-driven current profile. J Atmos Ocean Technol. https://doi.org/10.1175/JTECH-D-16-0090.1

Laxague NJM, Zappa CJ (2020) Observations of mean and wave orbital flows in the ocean's upper centimetres. J Fluid Mech 887:A10. https://doi.org/10.1017/jfm.2019.1019

Laxague NJM, Zappa CJ, LeBel DA et al (2018) Spectral characteristics of gravity-capillary waves, with connections to wave growth and microbreaking. J Geophys Res Oceans. https://doi.org/10.1029/2018JC013859

Lee YS, Han S, Park KC (2014) A scaling law for form drag coefficients in incompressible turbulent flows. Ocean Eng. https://doi.org/10.1016/j.oceaneng.2014.09.044

Lenain L, Melville WK (2017) Measurements of the directional spectrum across the equilibrium-saturation ranges of wind-generated surface waves. J Phys Oceanogr. https://doi.org/10.1175/JPO-D-17-0017.1

Lodise J, Özgökmen T, Griffa A et al (2019) Vertical structure of ocean surface currents under high winds from massive arrays of drifters. Ocean Sci Discuss. https://doi.org/10.5194/os-2019-16

Lund B, Haus B, Graber H et al (2020) Marine X-band radar currents and bathymetry: an argument for a wavenumber-dependent retrieval method. J Geophys Res Oceans. https://doi.org/10.1029/2019JC015618

Mahrt L, Nilsson E, Rutgersson A et al (2021) Vertical divergence of the atmospheric momentum flux near the sea surface at a coastal site. J Phys Oceanogr 51:3529–3537. https://doi.org/10.1175/JPO-D-21-0081.1

Makin VK, Kudryavtsev VN, Mastenbroek C (1995) Drag of the sea surface. Bound-Layer Meteorol 73(1–2):159–182. https://doi.org/10.1007/BF00708935

Monin AS, Obukhov AM (1954) Basic laws of turbulent mixing in the surface layer of the atmosphere. Tr Akad Nauk SSSR Geophiz 24(151):30

Morey SL, Wienders N, Dukhovskoy D et al (2018) Measurement characteristics of near-surface currents from ultra-thin drifters, Drogued drifters, and HF radar. Remote Sens 10(10):1633. https://doi.org/10.3390/rs10101633

Mueller JA, Veron F (2009) Nonlinear formulation of the bulk surface stress over breaking waves: feedback mechanisms from air-flow separation. Bound-Layer Meteorol 130(1):117–134. https://doi.org/10.1007/s10546-008-9334-6
NOAA NGDC (2003) U.S. coastal relief model - northwest pacific. https://doi.org/10.7289/V5H12ZXJ
Ortiz-Suslow DG, Kalogiros J, Yamaguchi R et al (2021) An evaluation of the constant flux layer in the atmospheric flow above the wavy air-sea interface. J Geophys Res Atmos. https://doi.org/10.1029/2020JD032834
Phillips OM (1985) Spectral and statistical properties of the equilibrium range in wind-generated gravity waves. J Fluid Mech 156(1):505
Plant WJ (1982) A relationship between wind stress and wave slope. J Geophys Res Ocean 87(C3):1961–1967. https://doi.org/10.1029/JC087IC03P01961
Plant WJ (2009) The ocean wave height variance spectrum: wavenumber peak versus frequency peak. J Phys Oceanogr 39(9):2382–2383. https://doi.org/10.1175/2009JPO4268.1
Plant WJ, Wright JW (1980) Phase speeds of upwind and downwind traveling short gravity waves. J Geophys Res 85(C6):3304. https://doi.org/10.1029/JC085iC06p03304
Prandtl L (1910) Eine beziehung zwischen wärmeaustausch and strömungswiderstand der flüssigkeiten. Z Physik 11:1072–1078
Renault L, McWilliams JC, Masson S (2017) Satellite observations of imprint of oceanic current on wind stress by air-sea coupling. Sci Rep 7(1):17–747. https://doi.org/10.1038/s41598-017-17939-1
Smeltzer BK, Æsøy E, Ådnøy A et al (2019) An improved method for determining near-surface currents from wave dispersion measurements. J Geophys Res Oceans. https://doi.org/10.1029/2019JC015202
Smith SD (1980) Wind stress and heat flux over the ocean in gale force winds. J Phys Oceanogr 10:18
Smith SD (1988) Coefficients for sea surface wind stress, heat flux, and wind profiles as a function of wind speed and temperature. J Geophys Res 93(C12):15–467. https://doi.org/10.1029/JC093iC12p15467
Smith SD, Banke EG (1975) Variation of the sea surface drag coefficient with wind speed. Q J R Meteorol Soc 101:8. https://doi.org/10.1002/qj.49710142920
Snyder RL, Dobson FW, Elliott JA et al (1981) Array measurements of atmospheric pressure fluctuations above surface gravity waves. J Fluid Mech 102:1–59. https://doi.org/10.1017/S0022112081002528
Spalding DB (1961) A single formula for the law of the wall. J Appl Mech 28(3):455–458
Stewart RH, Joy JW (1974) HF radio measurements of ocean surface currents. Deep-Sea Res 21:1039–1049. https://doi.org/10.1016/0011-7471(74)90066-7
Tennekes H (1973) The logarithmic wind profile. J Atmos Sci 30:234–238
Veron F, Saxena G, Misra SK (2007) Measurements of the viscous tangential stress in the airflow above wind waves. Geophys Res Lett 34(19):L19-603. https://doi.org/10.1016/0011-7471(74)90066-7
von Kármán T (1939) The analogy between fluid friction and heat transfer. Trans ASME 61:705–710
Wu J (1975) Wind-induced drift currents. J Fluid Mech 68(1):49–70. https://doi.org/10.1017/S0022112075000687
Wu J (1983) Sea-surface drift currents induced by wind and waves. J Phys Oceanogr 13(8):1441–1451.
Yelland M, Taylor PK (1996) Wind stress measurements from the open ocean. J Phys Oceanogr 26:18

Authors and Affiliations

David G. Ortiz-Suslow[1] · Nathan Laxague[2,6] · Jan-Victor Björkqvist[3] · Milan Curcic[4,5]

✉ David G. Ortiz-Suslow
dortizsu@nps.edu

[1] Department of Meteorology, Naval Postgraduate School, 589 Dyer Rd, Monterey, CA 93943-5114, USA

[2] Department of Mechanical Engineering, University of New Hampshire, 24 Colovos Road, Durham, NH 03824, USA

[3] Norwegian Meteorological Institute, Allegaten 70, 5007 Bergen, Norway

[4] Department of Ocean Sciences, Rosenstiel School of Marine, Atmospheric, and Earth Science,

University of Miami, 4600 Rickenbacker Causeway, Miami, FL 33149, USA

[5] Frost Institute for Data Science and Computing, University of Miami, 1552 Brescia Ave., Coral Gables, FL 33146, USA

[6] Center for Ocean Engineering, University ofNew Hampshire, 24 Colovos Road, Durham, NH 03824, USA